

Antiresonances in the Mid-Infrared Vibrational Spectrum of Functionalized Graphene

François Lapointe,^{†,‡,#} Bruno Rousseau,^{¶,#} Vincent Aymong,[¶] Minh Nguyen,[†]
Maxime Biron,[§] Etienne Gaufres,[†] Saman Choubak,[§] Zheng Han,^{||} Vincent
Bouchiat,^{||} Patrick Desjardins,[§] Michel Côté,^{*,¶} and Richard Martel^{*,†}

[†] *Département de chimie and Regroupement Québécois sur les Matériaux de Pointe,
Université de Montréal, C. P. 6128, Succursale Centre-Ville, Montréal, Québec H3C 3J7,
Canada*

[‡] *Now at: Security and Disruptive Technology Portfolio, National Research Council
Canada, 1200 Montreal Road, Ottawa, Ontario K1A 0R6, Canada*

[¶] *Département de physique and Regroupement Québécois sur les Matériaux de Pointe,
Université de Montréal, C. P. 6128, Succursale Centre-Ville, Montréal, Québec H3C 3J7,
Canada*

[§] *Département de génie physique and Regroupement Québécois sur les Matériaux de
Pointe, École Polytechnique de Montréal, C. P. 6079, Succursale Centre-ville, Montréal,
Québec H3C 3A7, Canada*

^{||} *Université de Grenoble, Alpes, Institut NÉEL, F-38042 Grenoble, France*

[⊥] *CNRS, Institut NÉEL, F-38042 Grenoble, France*

[#] *Contributed equally to this work*

E-mail: Michel.Cote@umontreal.ca; r.martel@umontreal.ca

Abstract

We report anomalous antiresonances in the infrared spectra of doped and disordered single layer graphene. Measurements in both reflection microscopy and transmission configurations of samples grafted with halogenophenyl moieties are presented. Asymmetric transparency windows at energies corresponding to phonon modes near the Γ and K points are observed, in contrast to the featureless spectrum of pristine graphene. These asymmetric antiresonances are demonstrated to vary as a function of the chemical potential and defect density. We propose a model which involves coherent intraband scattering with defects and phonons, thus relaxing the optical selection rule forbidding access to $\mathbf{q} \neq \Gamma$ phonons. This interpretation of the new phenomenon is supported by our numerical simulations that reproduce the experimental features.

1 Introduction

Graphene has found promising applications^{1,2} in plasmonics for the terahertz (THz) to mid-infrared (MIR) regime because of the optical properties pertaining to its bidimensional semimetallic nature.³ In this energy range, its absorption spectrum is dominated by a Drude-like response that can be modulated by doping.⁴ The optical response is, however, monotonous because there is no infrared-active phonon mode available, a fact explained by Zallen's rule stating that at least three atoms in the primitive unit cell are necessary (and sufficient) to generate infrared activity in an elemental crystal.⁵ Tailoring the optical response of single layer graphene (SLG) has therefore required creating plasmonic resonators and metamaterials by patterning the material into nanoribbons,⁶⁻⁸ nanodisks, heterostructure stacks,⁹ etc. In contrast, pristine bilayer graphene (BLG) demonstrates a native tunable Fano resonance,^{10,11} while BLG nanoribbons exhibit phonon-induced transparency through plasmon-phonon coupling.^{12,13}

A mode with no net dipole moment is known as a dark mode since it cannot interact directly with far field radiation. It may, however, be excited by the near field pertaining to a

bright mode, thus potentially resulting in quantum interference between the dark and bright states; the bright mode spectral response will then be modulated as a function of their phase difference, giving rise to a Fano lineshape.¹⁴ Mapping dark modes improves the knowledge of a system's levels and energy flow. Further, their existence sets favorable conditions for electromagnetic-¹⁵ or phonon-induced transparency, slow light¹⁶ and high local fields.¹⁷

The selection rules of light-matter interaction can be relaxed if the symmetry of the system is lowered or through higher order interplays like overtones and combination bands. Phenomena such as the Fermi resonance^{18,19} and the Rice effect²⁰ also come into play in certain systems. Apart from that, defects and impurities lift the translational invariance of the crystal giving access to phonon modes away from the center of the Brillouin zone.²¹ This effect gives rise to absorption bands in the infrared spectrum of otherwise transparent crystals such as diamond and silicon. Also, the Raman spectrum of sp^2 carbon materials presents numerous bands due to double resonance processes,²² which are enabled by the existence of two valleys in the electronic structure. In the presence of disorder induced by symmetry breaking defects, the Raman spectrum is further augmented by the D and D' bands, which also stem from double resonance processes. Such phenomena relying on intervalley scattering are of great interest in the emerging field of “valleytronics”, having stimulated proposals of applications such as valley valves and filters,²³ valley contrasting Hall transport²⁴ or valley dependent electron-polarized light interaction.²⁵ Experimental evidence of valley scattering phenomena is scarce^{26,27} and remains unreported in the MIR spectrum of graphene, although one would expect similar physics to occur.

We report on a novel scattering phenomenon mediated by phonons and disorder, and its manifestation in the MIR spectra of SLG. The infrared spectra of covalently functionalized graphene show Fano-like antiresonances which we demonstrate to emerge from scattering with randomly distributed grafts, thereby allowing momentum transfer between phonons and electronic intraband excitations.²⁸ The scattering process leads to sharp transparency windows in the mid-infrared optical conductivity at frequencies corresponding to optical

phonon energies for momenta near the Γ and $\pm K$ points, the latter being a direct consequence of intervalley scattering. The mechanism is reminiscent, but distinct, of the double resonance scattering process between the two Dirac cones of graphene, that leads to the occurrence of the D band in Raman spectroscopy of disordered samples.²⁹ The phenomenon appears ubiquitous to low dimension carbon structures such as carbon nanotubes,³⁰ and can potentially be exploited in optoelectronic applications in the infrared.

2 Experimental and theoretical methods

2.1 Samples preparation

2.1.1 Graphene growth

Graphene has been grown from a pulsed chemical vapour deposition (CVD) method on copper foil which produces predominantly single layer samples.³¹

2.1.2 Infrared microscopy samples

For the infrared microscopy measurements in reflection mode, PMMA-supported graphene is transferred through copper dissolution using 0.1 M $(\text{NH}_4)_2\text{S}_2\text{O}_8$ (98+%, Reagent grade, Acros Organics)³² on intrinsic silicon substrates (600 μm thickness, resistivity $> 5000 \Omega \text{ cm}$) with 300 nm thermal oxide bearing markers defined through photolithography. An electrode of Pd on top of a sticking layer of Ti (respectively 30 nm and 2 nm) was deposited at the edge to contact graphene electrically for subsequent electrografting. The procedure for electrografting graphene from in situ generated diazonium cations was adapted from the work of Baranton and Bélanger on glassy carbon³³ and Gan et al.³⁴ The electrode and bordering graphene was protected from the reacting solution with PTFE tape. 4-Iodoaniline (99%, Acros Organics) was dissolved in degassed acetonitrile (Certified ACS Plus, Fisher Scientific) to a concentration of 5 mM along with 0.1 M of tetrabutylammonium hexafluorophosphate (98%, Sigma-Aldrich) that served as the electrolyte. Diazonium cation was generated by the

addition of *tert*-butylnitrite (90%, Acros Organics) to a concentration of 10 mM. After a 5 minutes delay, the sample was connected to the potentiostat and voltamperometry cycles were started. The system was cycled 5 times between -0.4 and 0.4 V vs. Ag/AgCl reference electrode. After electrografting, the samples were rinsed abundantly in acetonitrile and 2-propanol.

2.1.3 Infrared transmission spectroscopy samples

The graphene samples that served for measurements in transmission spectroscopy were transferred to BaF₂ windows (Spectral Systems LLC, 40×20×4 mm). In this case, graphene was functionalized prior to transfer using two methods: First, for the samples used to test the dependency on doping, diazonium cations were generated in situ from a 1 mM 4-iodoaniline solution in acetonitrile to which *tert*-butylnitrite was added to a 10 mM concentration.³⁵ After a 5 minutes delay, while still supported on copper foil, the graphene sample was dipped in the reacting solution for 10 minutes. The grafting process ended by copiously rinsing in acetonitrile and 2-propanol. Pristine and grafted graphene samples (~ 1 cm²) were deposited side by side on the same BaF₂ windows for comparison. Second, to verify the influence of grafting density, we directly used 4-bromobenzenediazonium tetrafluoroborate at three different concentrations (10, 50 and 100 μ M) in acetonitrile. The samples supported on copper foil were immediately dipped in the reacting solution for 10 minutes, and finally rinsed with acetonitrile before being transferred to BaF₂ crystals.

2.1.4 Chemical doping

Doping was obtained by soaking the sample in a solution of the dopant at a given concentration in acetonitrile for 10 minutes, and subsequently drying the sample with a gentle stream of air. In microscopy measurements, 2,3-dichloro-5,6-dicyano-1,4-benzoquinone (DDQ, 98%, Sigma-Aldrich) at a 1 mM concentration was used to *p*-dope the samples. *N*-type doping being notoriously more difficult to achieve in air,^{36,37} a 10 mM hydrazine solution (diluted

from 35% w/V in water, Sigma-Aldrich) was used instead. The DDQ concentration was varied to verify the doping dependency by transmission measurements. Finally, in order to maximize the effect, the influence of grafting density was verified at a dopant concentration of 10 mM.

2.2 Samples characterization

2.2.1 Infrared microscopy

The infrared spectra in microscopy were acquired in reflection mode on a Hyperion 3000 infrared microscope (36 \times objective) coupled to a Bruker Vertex 80v Fourier transform spectrometer. We used a Globar source (aperture 3.5 mm), a KBr beamsplitter and a single channel, liquid nitrogen cooled mercury-cadmium-telluride (MCT) detector with a 250 \times 250 μm chip size (Bruker, D316-025). A total of 1024 scans were averaged at 40 kHz modulation frequency (HeNe laser) and a resolution of 4 cm^{-1} . A Blackman-Harris (3 terms) apodization function was applied at Fourier transform time, as well as a 2 \times zero filling level. In order to maximize the signal, we worked without knife-edge aperture, such that the effective aperture was defined by the projection of the detector element on the sample plane, i.e., a square of $\sim 65 \times 65 \mu\text{m}$.

The objective of the microscope was fitted with a small chamber purged with dry nitrogen to avoid spurious interferences from water vapor in the 1600 cm^{-1} spectral region. It was found necessary to use a prolonged purge time of at least 20 minutes to keep the rovibrational peaks of water vapor to a minimum. The reference single-beam spectrum I_0 was taken at a clean spot on the silicon substrate. Measurements were then acquired at identified areas with the help of markers for different doping levels (as is, *p*-type [DDQ]= 1 mM, *n*-type [hydrazine]= 10 mM), and for pristine and functionalized graphene with iodophenyl moieties. Finally, reflectance was computed as $R = I/I_0$, with I the single-beam spectrum of the sample.

2.2.2 Infrared transmission spectroscopy

Infrared transmissions spectra were performed on a Bruker Vertex 80v Fourier transform spectrometer equipped with a Globar source (aperture 500 μm), an extended domain KBr beamsplitter, and a liquid nitrogen cooled photoconducting MCT detector (Bruker, D316/B, chip size 1×1 mm). A total of 1024 scans were averaged at a HeNe laser modulation frequency of 40 kHz. A resolution of 4 cm^{-1} has been used, along with an Norton-Beer (medium) apodization function, and a zero filling factor of $4\times$. The spectrometer is held under rough vacuum (~ 1 torr). The sample compartment was pumped for 10 minutes before every measurements. The reference single-beam spectra I_0 were taken in a clean area of the BaF_2 windows. Transmittance is here defined as $T = I/I_0$, where I is the single-beam spectrum of the sample, and absorbance is given by $-\log T$.

2.2.3 Scanning electron microscopy

Pictures of selected and identified areas of the samples were acquired using a Hitachi S-4700 instrument, with a cold cathode as an electron source and a secondary electrons detector. An electron beam current of 10 μA at a 1 kV potential were used at a 5 mm working distance. These parameters were optimized to image graphene on SiO_2 by reduction of charging effects.

2.2.4 Raman microspectroscopy

Raman spectra were measured on a Renishaw RM-3000 instrument. The excitation laser was a Ar^2 ion source ($\lambda_{\text{ex}} = 514$ nm, power 25 mW). The diffraction grating had a 1800 lines/mm density, and we used a $50\times$ objective (NA= 0.55). The position of the grating was adjusted using the 520.7 cm^{-1} band of silicon within a variation of ± 0.5 cm^{-1} . The defect density was estimated using the D/G ratio after Lucchese et al.'s method.³⁸ Inspection of the spectra showed a loss of features for the samples used for the chemical doping experiments (reflection and transmission), which allowed us to conclude that L_D was smaller than 5 nm.³⁹ The defect density series spectra presented defined bands, thus indicating a L_D equal or higher than

5 nm.

2.2.5 Raman hyperspectral imaging

Raman maps were captured at an excitation wavelength of 532 nm using the hyperspectral imager RIMATM developed in collaboration between Prof. Martel's research group and Photon etc. Ltd society. The acquisition parameters were the following: 100× objective, laser power density $80 \mu\text{W} \mu\text{m}^{-2}$, and an acquisition time of 120 seconds per pixel. The images are 512×512 pixels with a binning level of 2, thus yielding an image size of $130 \times 130 \mu\text{m}$. The measurement data set is tridimensional, whereas every pixel in space plane has a related complete spectrum in the spectral domain specified by the operator.

2.2.6 X-ray photoelectron spectroscopy

The X-ray photoelectron spectroscopy (XPS) measurements were performed under high vacuum ($\sim 10^{-9}$ torr). An aluminium cathode was used as a source of X-rays at a 12.5 kV potential and a 140 W power. Incidence angle was set at 45° . The survey spectra were acquired at binding energies ranging from 1233 eV to 10 eV, in 1 eV increments with a pass energy of 100 eV. High resolution spectra were done in a restricted domain using 0.1 eV increments and a passing energy of 10 eV. Atomic ratios were automatically calculated using the CasaXPS software.

2.3 Modeling

The contribution of Eq. (3) to the optical conductivity was computed within the tight-binding approximation in the spirit of the work of Peres et al.⁴⁰ Impurity scattering is modeled in terms of on-site, randomly located impenetrable potentials, treated in a way to make use of the Full Born Approximation.⁴⁰ The phonon frequencies and polarization vectors were obtained from a force constant model;⁴¹ the phonon dispersion was modified in the vicinity of $\pm K$ to account for the physically well established Kohn anomalies at these points,⁴² but

which the force constant model fails to capture. The parameters entering the electron-phonon coupling matrix elements were obtained by comparing with computed results available in the literature at $\mathbf{q} = \Gamma$ and $\mathbf{q} = K$ ^{42,43} (see Supporting Information). Simulations were conducted using an in-house computer program built explicitly for this purpose.

3 Results

Our samples consist of SLG grown on copper foil using a specific intermittent growth chemical vapor deposition (CVD) process that allows production of a fully homogeneous monolayer without multilayer patches.³¹ The graphene thus obtained was then transferred to a MIR transparent substrate (oxidized intrinsic silicon or BaF₂) with regular transfer techniques.³² The graphene sheets have been fully characterized through optical and scanning electron microscopy, along with Raman microspectroscopy and hyperspectral cartography to ensure that there is no bilayer contamination within the investigated regions (see Supporting Information). Covalent functionalization is then used to introduce disorder in the crystalline lattice [Fig. 1(a)].³³⁻³⁵ Indeed, grafting of iodophenyl moieties (I-Ph) to graphene breaks the sp^2 conjugation and generates sp^3 hybridized scattering centers.⁴⁴ The reaction, however, leaves the samples in a state where the Fermi level is poorly defined from adsorbed ions and grafts. We thus use chemical doping to set the chemical potential. Practically, this is achieved by soaking the sample in a doping solution at a certain concentration, and then drying in a stream of nitrogen, which leaves the adsorbed dopant molecules on the surface. For instance, 2,3-dichloro-5,6-dicyano-1,4-benzoquinone (DDQ, an electron acceptor) dissolved in acetonitrile is used for p -type doping, while hydrazine (an electron donor) in acetonitrile allows reduction of graphene.

Infrared spectroscopy measurements are displayed in Fig. 1(b) and Fig. 2(b). The first set of data presented in Fig. 1(b) shows the results of microscopy measurements in reflection mode of SLG transferred onto intrinsic silicon with 300 nm thermal oxide, which allowed us to

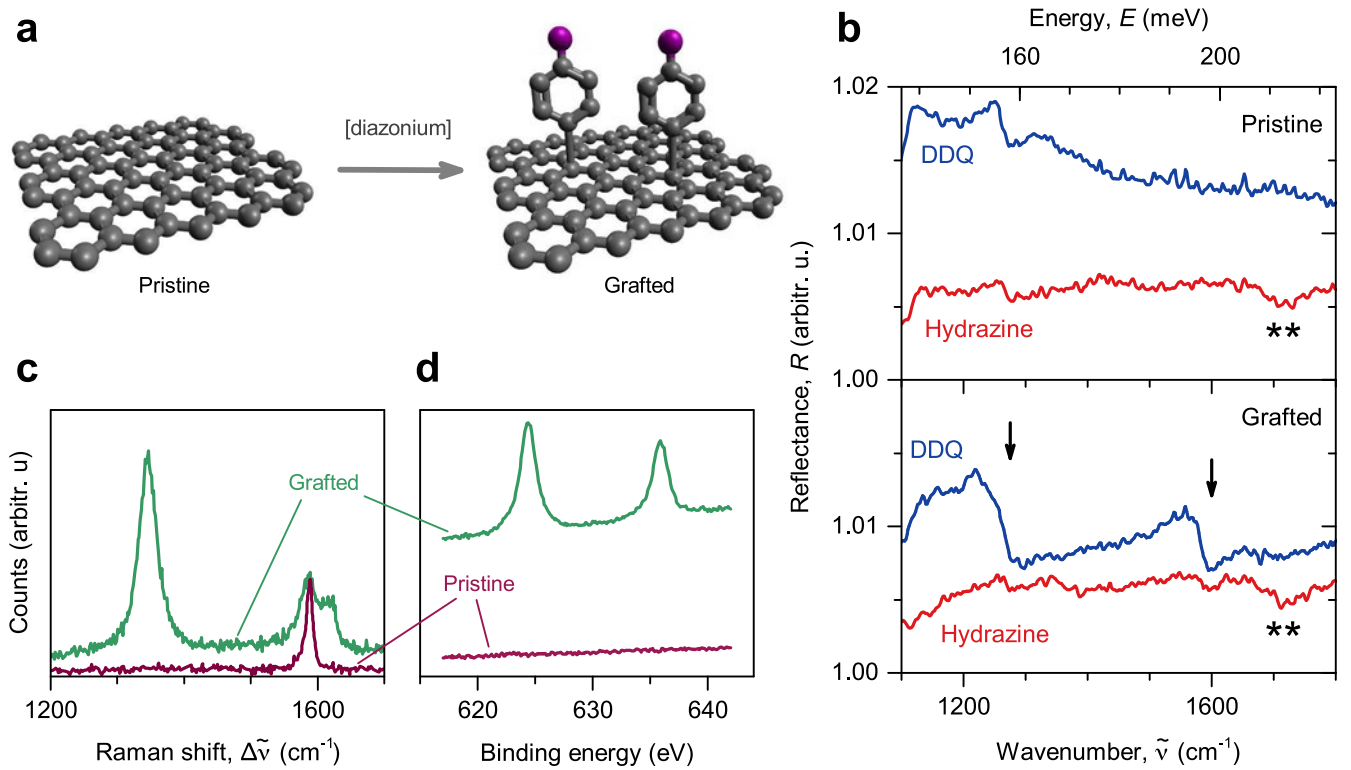


Figure 1: (a) Schematics of the functionalization of SLG using diazonium chemistry. (b) Mid-infrared reflection spectra in microscopy of pristine (upper panel) and electrografted SLG (lower panel) transferred onto 300 nm thermal oxide grown onto an intrinsic silicon wafer. Spectra are shown after soaking in dopant solutions of $[\text{DDQ}] = 1 \text{ mM}$ and $[\text{hydrazine}] = 10 \text{ mM}$ in acetonitrile. (c) Typical Raman spectra at $\lambda_{\text{ex}} = 514 \text{ nm}$ for pristine and grafted SLG. The data has been normalized to the G band. (d) Typical XPS traces in the iodine $3d_{5/2}$ and $3d_{3/2}$ region for pristine and grafted SLG.

probe well characterized regions of the sample and to exclude areas with bilayer and few-layer islands. Except for a weak modulation near 1250 cm^{-1} and the carbonyl band of an impurity at $\sim 1720\text{ cm}^{-1}$ (denoted by **), pristine graphene yields a featureless MIR spectrum in both doping states (i.e., $[\text{DDQ}] = 1\text{ mM}$ and $[\text{hydrazine}] = 10\text{ mM}$) [Fig. 1(b), top panel]. This behavior is expected since no graphene phonons are supposed to be infrared-active.⁴⁵ In accordance with our following arguments, the weak modulation near 1250 cm^{-1} may be due to the fact that the probed area contains wrinkles and joint boundaries between crystal domains (see microscopy pictures in Supporting Information), which are sources of disorder. The observations, however, change drastically upon covalent grafting to graphene: As seen in the bottom panel of Fig. 1(b), a broad asymmetric signal is now apparent near 1600 cm^{-1} in the DDQ-doped trace, and a second, even broader signal is also observed around 1250 cm^{-1} . Vibrational bands from dopants and I-Ph are absent from the MIR spectra because their concentrations are lower than the detection limit. Moreover, the asymmetric bands disappear upon soaking in a hydrazine solution, and can be recovered by doping back to *p*-type (see Supporting Information), thus demonstrating a dependency on charge carrier density.

Fig. 1(c) and (d) show typical traces of pristine and grafted SLG in Raman spectroscopy and X-ray photoelectron spectroscopy (XPS), respectively. The graft density is evaluated by iodine content analysis by XPS to approximately 1 I-Ph for 100 C atoms, which is corroborated by analysis of the Raman D/G ratio using Lucchese et al.'s method (see Supporting Information).^{38,39}

The optical window of silicon dioxide (SiO_2) being limited in the infrared by an intense absorption band at $\sim 1050\text{ cm}^{-1}$, transmission spectra were obtained on a BaF_2 substrate to better assess the graphene band observed at $\sim 1250\text{ cm}^{-1}$. In these measurements, macroscopic sample areas were probed to prove that the effect is not limited to localized microscopic regions. This second set of data is shown in Fig. 2 using an optical conductivity scale for pristine graphene doped at $[\text{DDQ}] = 1\text{ mM}$, and for grafted graphene (graft density of approximately 2 I-Ph for 100 C atoms as evaluated by XPS and ca. 1 defect for 100 C

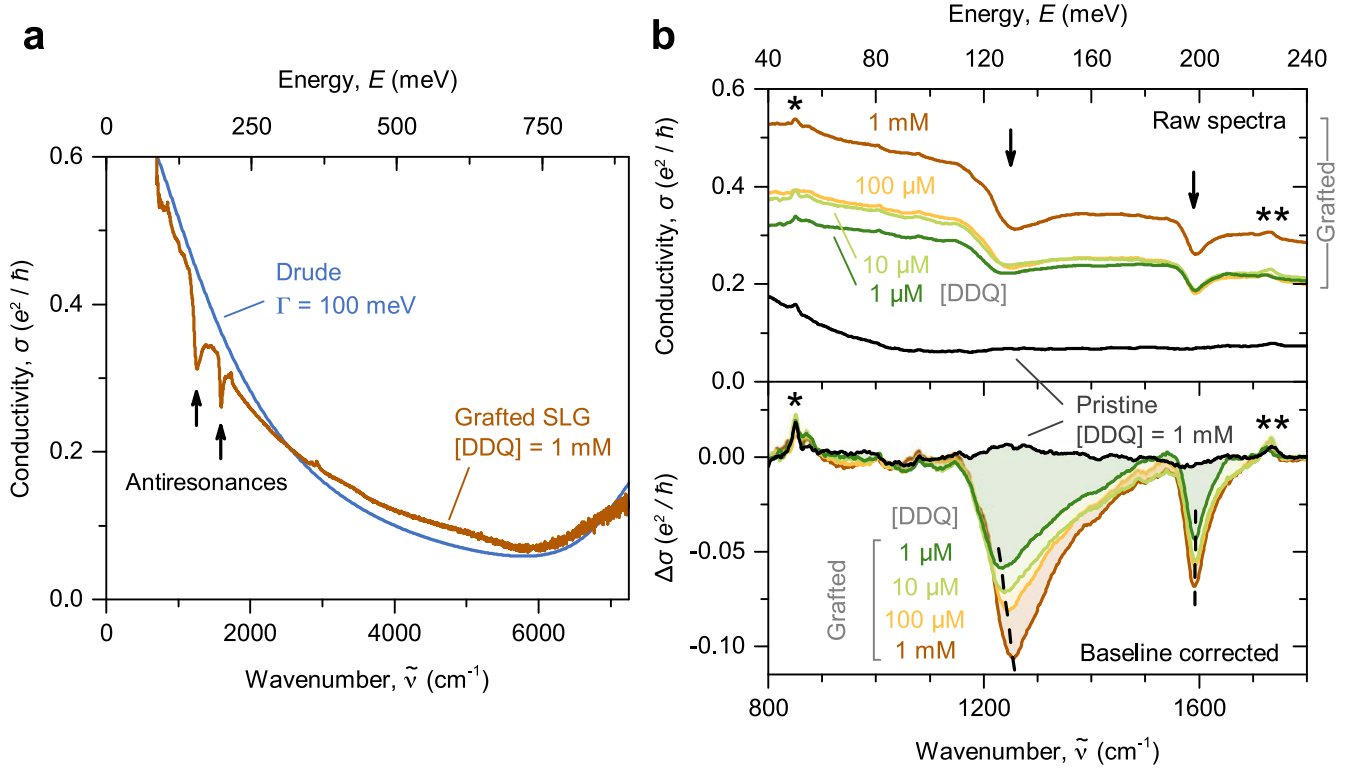


Figure 2: (a) Mid-infrared optical conductivity of grafted SLG doped at $[\text{DDQ}] = 1 \text{ mM}$ on BaF_2 measured in transmission on top of the calculated Drude conductivity for $\Gamma = 100 \text{ meV}$ at $\mu = -450 \text{ meV}$. (b) Experimental data of pristine and grafted SLGs on BaF_2 at different doping concentrations. Raw spectra are presented in the upper panel, while the lower panel shows traces after subtraction of a cubic baseline. The trace in black is the pristine sample doped at $[\text{DDQ}] = 1 \text{ mM}$ and the other traces belong to a functionalized sample for varying DDQ concentrations. The arrows show the disorder-induced antiresonances, while the star (*) denotes a spurious band, and the double stars (**), the carbonyl band of an impurity.

atoms by Raman spectroscopy) *p*-doped at various levels (from [DDQ]= 1 μ M to 1 mM). The wide experimental spectrum of grafted graphene doped with [DDQ]= 1 μ M has been singled out in Fig. 2(a) and plotted against the calculated Drude conductivity showing good agreement, except for the presence of two antiresonances. Raw spectra corresponding to the doping series are presented in the top panel of Fig. 2(b), while all spectra in the lower panel have been corrected with a cubic baseline to account for experimental background, which includes a Drude contribution, as seen in Fig. 2(a). The two antiresonances are identified at ~ 1250 cm^{-1} and ~ 1600 cm^{-1} , whereas the pristine signal (black trace) is smooth, to the exception of a spurious band denoted by a star (*), and the carbonyl band of an impurity marked by double stars (**). The frequencies of the antiresonances coincide with those of the Raman *D* and *G* bands, thus strongly suggesting that phonon modes are involved in the mechanism.

The profiles of the antiresonances are asymmetric and skewed toward higher energies, and as such they can be modeled with a phenomenological Fano profile (see fits and fitting parameters in Fig. S10 and Tables S1-2 of the Supporting Information, respectively). The estimated Fano linewidths for the low energy mode range from 130 to 174 cm^{-1} , while the linewidths of the high energy mode extend from 37.0 to 49.5 cm^{-1} . The estimated Fano linewidths for the low energy mode range from 130 to 174 cm^{-1} , while the linewidths of the high energy mode extend from 37.0 to 49.5 cm^{-1} . In comparison, the Raman linewidths for the same samples in an undoped state are (24 ± 4) cm^{-1} for the *G* band of the pristine sample, (40 ± 6) cm^{-1} for both the *G* and the *D* bands of the functionalized sample, and a value of ca. 15 cm^{-1} has been reported for the Raman *G* band of pristine SLG at 200 K.⁴⁶ Another important observation is the modulation of the amplitude of the MIR anomalies with dopant concentration, which becomes evident after baseline correction [Fig. 2(b), bottom panel]. As can be observed in the top panel, the background absorption also evolves following the known dependence of the Drude peak to doping,⁴ thus supporting the fact that the signal cross section is related to charge carrier density. It should be stressed that the observed

transparency windows (antiresonances) are important hints about the underlying mechanism, since it is in discrepancy with normal phonon resonances, which absorb light and thus would yield upward bands on a conductivity scale.

3.1 Extension to the Drude model

To first gain intuition about the mechanism underpinning the occurrence of the antiresonances, we begin by extending the Drude model to collisions between a representative semi-classical electron and a phonon mode. Requiring only momentum and energy conservation, we derive the following expression for the conductivity σ (Sec. 2.1, Supporting Information):

$$\text{Re}[\sigma(\omega)] \simeq \sigma_0 \frac{(2\Gamma)^2}{(2\Gamma)^2 + (\hbar\omega)^2} + \Delta\sigma(\omega) \quad (1)$$

$$\frac{\Delta\sigma(\omega)}{\sigma_0} \propto \frac{m}{M} \text{Im} \left[\frac{(2\Gamma)^3}{(\hbar\omega + 2i\Gamma)^2} \mathcal{D}_{\text{ph}}(\omega) \right], \quad (2)$$

where σ_0 is the static Drude conductivity, m/M is the ratio of electronic to ionic mass, 2Γ is the width of the Drude peak and $\mathcal{D}_{\text{ph}}(\omega)$ is the Green function of the phonon mode, which is sharply peaked at the frequency of the phonon. The first term in Eq. (1) is the familiar Drude conductivity, while the second term accounts for an interference effect induced by multiple subsequent electron-phonon scattering events and the dynamical nature of the phonon. For $\hbar\omega > 2\Gamma$, where $\hbar\omega$ is the energy of the incoming infrared photon and Γ is the width of the Drude peak, this simple model reproduces asymmetric antiresonances skewed toward higher energies and centered at the phonon frequency (Fig. S16, Supporting Information). While this simple extension to the Drude model gives an intuitive picture for the underlying physics at play, it is not sufficient to account for the quantum mechanical nature of electrons and phonons, nor does it take into consideration selection rules or band dispersion. Hence, a more elaborated model is required.

3.2 Quantum mechanical model

A proper treatment of the optical conductivity makes use of the Kubo formula,⁴⁷ which relates $\sigma(\omega)$ to the current-current correlation function. The effects of electron-phonon coupling as well as defect scattering can then be computed systematically using the machinery of perturbation theory and Feynman diagrams, an approach which treats both intraband and interband electronic excitations on equal footing (for an introductory presentation of Feynman diagrams, see the guide by Mattuck⁴⁸). The quantum mechanical mechanism corresponding to the classical model of Eq. (1) is described by the Feynman diagram of Fig. 3(a) in the case where *intraband* electronic excitations (i.e., excitations near the Fermi energy) dominate. This same Feynman diagram, but with an emphasis on *interband* electronic excitations, was first proposed by Cappelluti et al.^{49,50} to explain the Fano profile observed in pristine bilayer graphene^{10,11} and few-layer graphene,⁵¹ where a discrete mode (a tangential phonon mode at Γ) couples to the continuum of electron-hole excitations responsible for an optical resonance. This mechanism was also applied to plasmon-phonon coupling to account for similar observations in BLG nanoribbons.¹² In pristine SLG, however, a Fano resonance has never been observed, nor is it expected: indeed, the contribution from the mechanism of Fig. 3(a) vanishes by symmetry. Even more, the other observed band at $\sim 1250 \text{ cm}^{-1}$ cannot be attributed to coupling to Γ point phonons, as there are no available phonon modes near this energy.

A key point to correctly model the observed phenomenon is the introduction of lattice defects (I-Ph grafting), which destroys the periodicity of the system. Its simplest consequence is a reduction of the electronic lifetime, leading to a broader Drude peak. However, the introduction of electronic damping in the mechanism of Fig. 3(a) still leads to an expression which vanishes by symmetry in SLG; the effect of disorder must thus be treated beyond the reduction of electronic lifetime. Averaging the current-current correlation function over all possible graft configurations, the simplest disorder contribution coupling non- Γ phonons to electronic excitations is given by the Feynman diagrams of Fig. 3(b) and (d). It is shown in

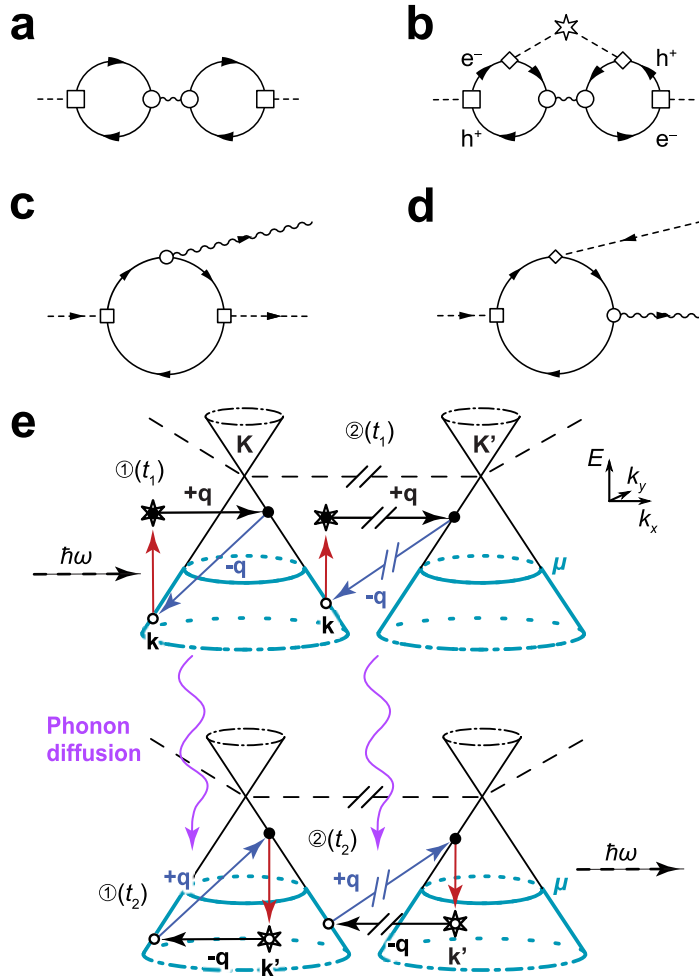


Figure 3: Feynman diagrams: (a) Electronic excitation with phonon scattering. Contribution to the current-current correlation function, which leads to a Fano profile in BLG but vanishes identically in SLG. (b) Defect scattering included. (c) Single phonon Raman scattering resonance. (d) Loop function. (e) Schematics of two of the possible resonant scattering mechanisms for ① intra- and ② intervalley processes.

the Supporting Information that it yields a contribution to the conductivity of the form

$$\text{Re} \left[\sigma_{\text{imp}}(\omega) \right] \simeq \frac{e^2}{\hbar} (n_{\text{imp}} a_0^2) \sum_{\alpha=x,y} \sum_{L=A,B} \frac{1}{N} \sum_{\nu\mathbf{q}} A_{\nu\mathbf{q}}^{\alpha L} \frac{|Q_{\nu\mathbf{q}}^{\alpha L}|^2 - 1 + 2z_{\nu\mathbf{q}} \text{Re} \left[Q_{\nu\mathbf{q}}^{\alpha L} \right]}{|Q_{\nu\mathbf{q}}^{\alpha L}|^2 (z_{\nu\mathbf{q}}^2 + 1)}, \quad (3)$$

with

$$z_{\nu\mathbf{q}} \equiv \frac{\hbar\omega - \hbar\omega_{\nu\mathbf{q}}}{\Gamma_{\nu\mathbf{q}}}, \quad (4)$$

where N is the number of unit cells in the sample, n_{imp} is the number density of defects, a_0 is the Bohr unit of length, $-e$ the electronic charge, α and L are related to the spatial direction of the current operator (x or y) and the defect scattering site in the graphene unit cell (A or B). Also, ν is a phonon mode label and \mathbf{q} is a momentum restricted to the First Brillouin zone; thus $\omega_{\nu\mathbf{q}}$ is the frequency and $\Gamma_{\nu\mathbf{q}}$ is related to the lifetime of the phonon labelled by $(\nu\mathbf{q})$. The contribution to the conductivity of Eq. (3) is composed of a sum over the whole first Brillouin zone of Fano-like terms with unitless parameters $Q_{\nu\mathbf{q}}^{\alpha L}$ and amplitudes $A_{\nu\mathbf{q}}^{\alpha L}$. These parameters are related to the mathematical expression corresponding to the diagram presented in Fig. 3(d), itself an important subpart of the full diagram presented in Fig. 3(b) (this expression is discussed at length in the Supporting Information). We name the expression in Fig. 3(b) the “loop” function, which we denote by $\mathcal{H}_{\nu\mathbf{q}}^{\alpha L}$, and we choose to represent it as the sum of “reactive” and “absorptive” terms,

$$\mathcal{H}_{\nu\mathbf{q}}^{\alpha L} = \mathcal{R}_{\nu\mathbf{q}}^{\alpha L} + i\mathcal{I}_{\nu\mathbf{q}}^{\alpha L}. \quad (5)$$

With this choice, the Fano parameter and amplitude take the simple form, in atomic units,

$$Q_{\nu\mathbf{q}}^{\alpha L} \equiv -\frac{\mathcal{R}_{\nu\mathbf{q}}^{\alpha L}}{\mathcal{I}_{\nu\mathbf{q}}^{\alpha L}} \quad \text{and} \quad A_{\nu\mathbf{q}}^{\alpha L} \equiv \frac{1}{\hbar\omega_{\nu\mathbf{q}}} \frac{1}{4\Gamma_{\nu\mathbf{q}}} \left| \mathcal{R}_{\nu\mathbf{q}}^{\alpha L} \right|^2. \quad (6)$$

The resonant transition in the loop function imposes that both momenta \mathbf{k} and $\mathbf{k} +$

\mathbf{q} should be within $\hbar\omega$ of the Fermi energy. If the chemical potential μ is small enough for the cone approximation to be valid, and provided that grafting does not break this approximation, then the Fermi surface is composed of circles of radius $k_\mu = |\mu|/\hbar v_F$ centered at $\pm K$ (where v_F is the Fermi velocity of graphene). For $\hbar\omega < |\mu|$, the resonance condition can only be satisfied for $\omega/v_F \leq |\mathbf{q}-\mathbf{P}| \leq 2k_\mu + \omega/v_F$, where $\mathbf{P} = \Gamma$ for \mathbf{q} near Γ and $\mathbf{P} = \pm K$ for \mathbf{q} near $\pm K$. For \mathbf{q} not satisfying the resonance condition, we expect nonresonant (and thus small) contributions to the current-current correlation function. Thus, although the sum in Eq. (3) is over the whole Brillouin zone, the resonance conditions lead to enhanced contributions for \mathbf{q} near Γ and $\pm K$ [see discussion below related to Fig. 4(b)].

The two steps illustrated in Fig. 3(e), namely the absorption (top panel) and emission (bottom panel) of a photon, summarizes the main features of this light-matter interaction for both intra- and intervalley scatterings. In a first step t_1 , an electron scatters on a defect after the absorption of a photon. The energy of the photon $\hbar\omega$ and the momentum \mathbf{q} imparted by the scattering event match those of an emitted phonon. The phonon is reabsorbed in a second step t_2 launching the reverse cycle of step t_1 and ending with the emission of a photon of energy $\hbar\omega$. The sum is a loop function that activates a resonant channel at the phonon frequency in a way that is analogous to the boomerang model⁵² used to describe resonance cross sections for the vibrational excitation of molecules bombarded by electrons. Here, the consequence is that the boomeranging electrons are unavailable for Drude scattering and hence cannot participate to photon absorption, leading to well-defined transmission windows or antiresonances reported here in the MIR absorption of graphene.

3.3 Validation of the model

We sought to validate the model first by simulating the optical conductivity, then by verifying a predicted feature of the theory, namely the influence of the graft density on the infrared response. In order to test the quantitative validity of the model, the contributions were computed for various chemical potential values μ at a graft density of 2%, a phonon energy

broadening $\Gamma_{\nu\mathbf{q}} = 2.5$ meV, and an electronic energy broadening $\Gamma = 75$ meV (as exposed in Sec. 2.2 of the Supporting Information, we estimate $\mu \simeq -450$ meV).

The model conductivity of Eq. (3) is compared in Fig. 4 to the experimental conductivity in the presence of disorder and after doping with 1 mM DDQ solution. The model reproduces the position and asymmetry of the two prominent bands in the baseline-corrected signal, and yields a roughly correct amplitude, given the uncertainty on the experimental chemical potential and Drude peak width. Also, it correctly captures the *transmission windows* signal profile (i.e., downward bands in the optical conductivity, upward bands on a transmittance scale) due to an interference effect between electron and phonon degrees of freedom. Finally, the contribution of the model to the conductivity vanishes as $\mu \rightarrow 0$, in agreement with the experimental observation that the asymmetric bands disappear upon soaking in hydrazine solution. For completeness, the conductivity was also computed for various reasonable values of the broadening parameter Γ : the asymmetry of the bands follows the same trend as that of the simple Drude-like model of Eq. (1), even when disorder is treated beyond lifetime effects [See Fig. S16 and S17(b) of the Supporting Information].

Following Cappelluti et al., we define the phonon coupling strength,⁵⁰

$$P_{\nu\mathbf{q}} \equiv \frac{1}{4} \sum_{\alpha=x,y} \sum_{L=A,B} \frac{1}{\hbar\omega_{\nu\mathbf{q}}} \left(\left| \mathcal{R}_{\nu\mathbf{q}}^{\alpha L} \right|^2 + \left| \mathcal{I}_{\nu\mathbf{q}}^{\alpha L} \right|^2 \right), \quad (7)$$

as a measure of the weight of the mode. Fig. 4(b), (c) and (d) show that the phonon coupling strength (red areas) is substantial only near the regions where the resonance conditions are satisfied (grey bands). This behavior leads to a coupling strength density of states with two major peaks corresponding to contributions coming from $\mathbf{q} \simeq \pm \mathbf{K}$ and $\mathbf{q} \simeq \Gamma$, as plotted in Fig. 4(a) (top panel, right axis). We note that the relative intensities of the antiresonances in the simulation are opposite to those of the experimental data. This discrepancy seems to stem from the phonon coupling strength which may be underestimated at lower energies. While we have successfully simulated the experimental spectra using purely calculated values,^{42,43}

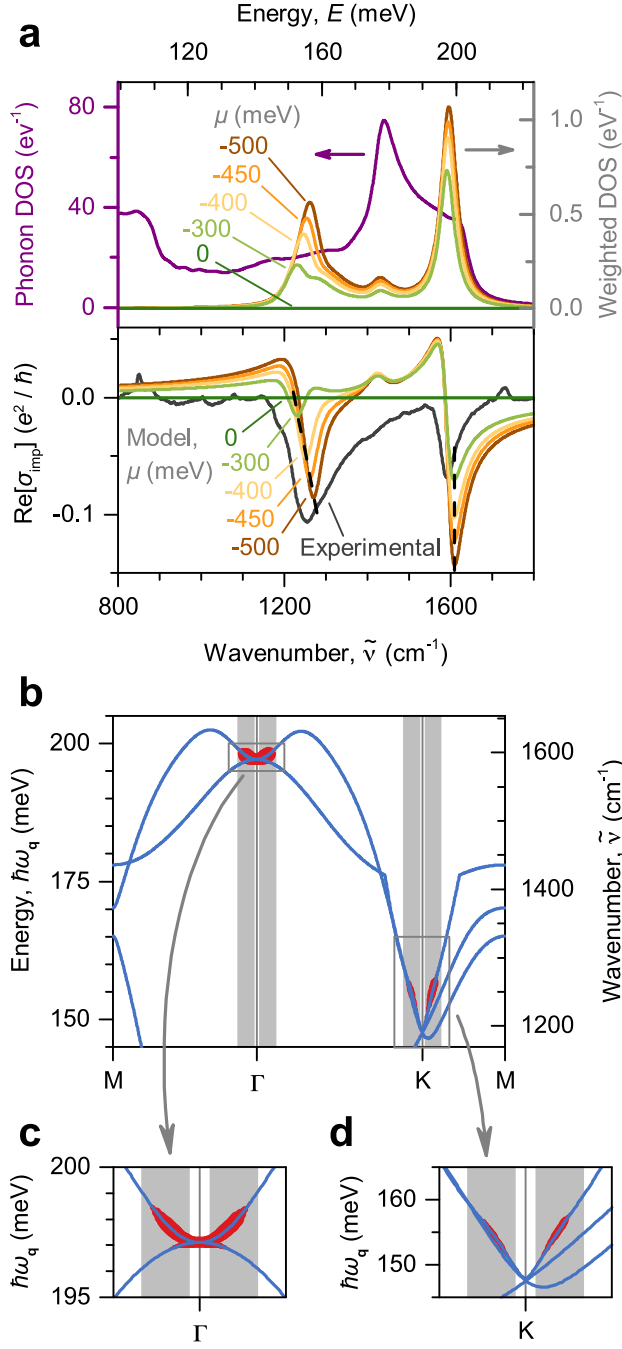


Figure 4: (a) Upper panel: Computed phonon density of states (purple trace, left axis), and density of states weighted with the phonon coupling strength $P_{\nu\mathbf{q}}$ for various chemical potential μ values (green to red traces, right axis). Lower panel: Computed contributions to the conductivity for various chemical potential values (colored traces), compared to experimental data corresponding to $[\text{DDQ}] = 1$ mM (dark grey trace). The dashed lines are tracking the minima for emphasis. (b) Model phonon dispersion of graphene (thin blue lines) overlaid with the phonon coupling strength (thick red regions): the region size is proportional to the corresponding $P_{\nu\mathbf{q}}$ value. The vertical grey bands indicate sections of the first Brillouin zone where the resonance conditions are satisfied for $\hbar\omega = 200$ meV with the chemical potential μ set to -450 meV and the energy zero corresponds to the Dirac point. Zoom of the regions near the (c) Γ point and (d) K point.

refinements of the calculations are to be expected now that we have devised an experimental and theoretical method that can lead to the extraction of electron-phonon coupling values.

The disorder contribution to the conductivity is expressed by Eq. (3), which shows $\text{Re}[\sigma_{\text{imp}}(\omega)]$ to be linearly dependent on n_{imp} , the number density of defects. We tested this prediction qualitatively by measuring the MIR spectra of SLG samples subjected to bromophenyl radical functionalization for 10 minutes at three different concentrations of 4-bromobenzenediazonium tetrafluoroborate (diazonium). Fig. 5(a) displays the resulting MIR spectra at a constant dopant concentration of $[\text{DDQ}] = 10 \text{ mM}$, and (b) presents an example of the scanning tunnelling microscopy (STM) images used to evaluate the density and distribution of grafted sites (seen as the white dots), which appear randomly over the entire surface. A higher diazonium salt concentration effectively yielded a higher defect density, as supported by Raman and STM measurements (see Supporting Information). As expected from a simple Drude model, the background signal [Fig. 5(a), top panel] rises linearly with increasing defect density (as determined by Raman spectroscopy) for at least the data points considered here, which are of 0.006% ($[\text{diazonium}] = 10 \text{ mM}$), 0.01% (50 mM) and 0.03% (100 mM), respectively. In qualitative agreement with our quantum mechanical model, the induced transparency is increased with the defect density, which appears clearly after subtraction of the baseline [Fig. 5(a), lower panel and Fig. S15]. The different protocols for the grafting of molecules used here lack of control at higher densities and improved methods will be needed to conclusively characterize the dependency of the amplitude at large grafting levels.

4 Discussion

The two prominent antiresonances in the experimental data can be readily explained. The feature at $\sim 1600 \text{ cm}^{-1}$ comes from coupling to phonons near the E_{2g} mode for $\mathbf{q} \sim \Gamma$ [process ① in Fig. 3(e)]; in agreement with experiments, the amplitude of the simulated

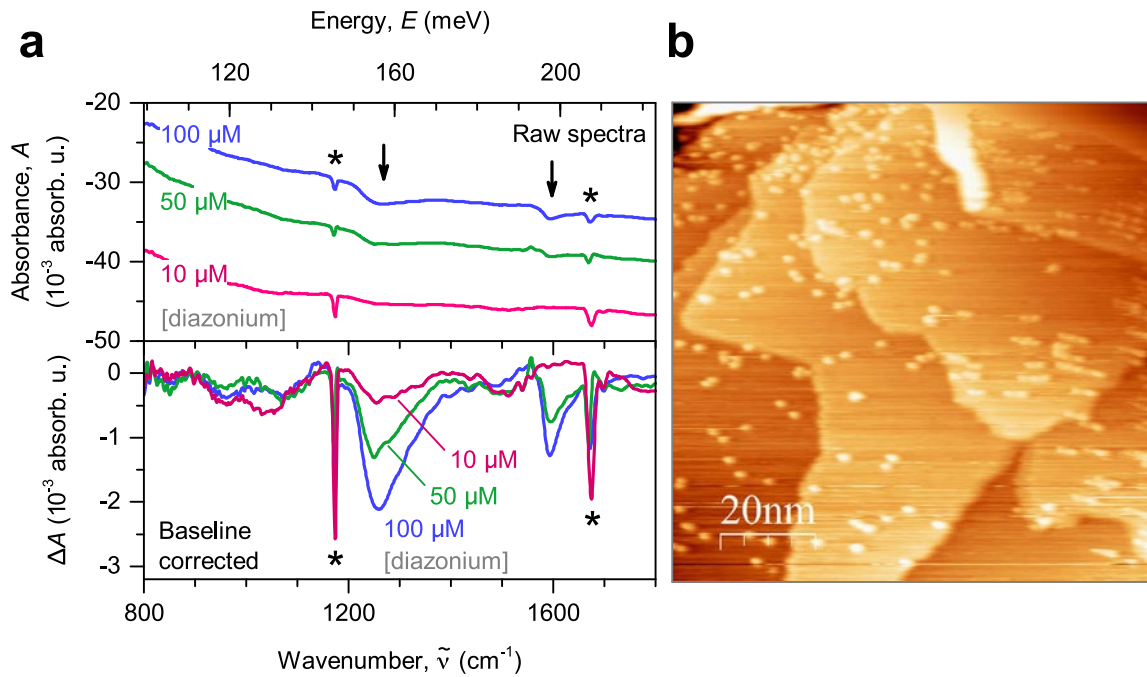


Figure 5: The influence of graft density on the MIR absorbance spectra of SLG. (a) MIR absorbance measured in transmission. The concentrations marked on the figure correspond to the respective concentration of diazonium salt used in the grafting process. The samples are supported on a BaF_2 substrate and doped with a $[\text{DDQ}] = 10 \text{ mM}$ solution. The raw and baseline corrected spectra are presented in the upper and lower panels, respectively. The antiresonances are marked with arrows, while the stars (*) flag vibrational modes of DDQ. (b) A typical STM image ($V_{\text{sample}} = 0.5 \text{ V}$ and $I = 0.08 \text{ A}$) of the sample functionalized using 100 mM of diazonium. A graft density (white dots) of 0.05% coverage is visible in the image.

band increases with $|\mu|$, while the position of the band remains unchanged, reflecting the lack of phonon dispersion near the E_{2g} mode at Γ . The broad feature in the vicinity of 1200-1400 cm^{-1} comes from coupling to phonons near the A'_1 mode for $\mathbf{q} \sim \pm K$ [process ② in Fig. 3(e)]; again, the simulated amplitude of the band increases with $|\mu|$ as observed experimentally, and its position moves to higher energy with $|\mu|$ [dashed line in Fig. 4(a) tracking the position of the minimum], a consequence of the strong phonon dispersion near the Kohn anomaly at $\pm K$. The large width of the low energy antiresonance, as compared to the higher energy mode, is also attributable to the steepness of the phonon dispersion near the K point. As seen in Fig. 4(b), (c) and (d), the red regions show the momentum-energy domains where phonon coupling is maximum. The maximal coupling region near the Kohn anomaly is indeed spread in energy about three times as much as near the Γ point. We note the absence of features around $\sim 1050 \text{ cm}^{-1}$, the frequency of the A'_2 mode at $\pm K$: this absence is consistent with simulations based on density functional theory suggesting that the electron-phonon coupling strength of this mode is negligible.⁵³

It is useful at this point to consider further the mechanisms illustrated in Fig. 3(a) and (b) for the gated BLG^{10,11,49} and for functionalized SLG, respectively. The case of gated BLG, which response function corresponds to the Feynman diagram pictured in Fig. 3(a), involves the interference between a continuum of electronic interband excitations and a discrete infrared-active phonon mode of the BLG located at Γ . Because the continuum of excited electronic states and the IR excited vibrational state are both optically allowed and coupled by electron-phonon interactions, a Fano resonance is observed in BLG, even without defect. In contrast, our experiments bring to light a disorder- and phonon-mediated interference phenomenon in SLG, which is at the origin of the transmission windows seen at frequencies matching infrared-forbidden phonon modes at $\mathbf{q} \sim \Gamma$ and $\mathbf{q} \sim \pm K$. In addition to the contribution leading to Fano resonances in pristine BLG, the proposed mechanism invokes additional *intraband* processes beyond lifetime effects and mediated by a defect and a phonon: an electron/hole pair in a state near the Fermi energy that scatters coherently

on a defect and a phonon, thus breaking the optical selection rule (i.e., $\mathbf{q} = \Gamma$) valid in pristine samples. Whereas Fano profiles are induced by a *discrete state-continuum* coupling between Γ phonon modes and electronic degrees of freedom, the new mechanism involves *continuum-continuum* coupling with phonon momenta constrained to small regions near Γ and $\pm K$.

Interestingly, the current-current correlation function shares strong similarities with the resonant single phonon Raman scattering process [diagram, Fig. 3(c)]. That is, the whole scattering process is resonant with an optical phonon mode in both momentum and energy, which is similar to a Raman resonant transition. Furthermore, defects allow for both intra- and intervalley processes involving small or large \mathbf{q} phonon modes (e.g. Raman D band at $\sim 1250 \text{ cm}^{-1}$). However, two major differences set them clearly apart: our proposed mechanism follows overall an elastic scattering path, whereas resonant Raman is inelastic by nature; the incoming light in Raman spectroscopy is energetic enough to induce interband transitions, whereas infrared light cannot in doped graphene, thus the resonant transition in the loop function imposes that both momenta \mathbf{k} and $\mathbf{k} + \mathbf{q}$ be within $\hbar\omega$ of the Fermi energy.

5 Conclusions

The reported phenomenon may prove useful in quantifying disorder in graphene, and it will allow the modulation of the optical conductivity in a narrow terahertz band, hence providing extended tools for telecommunications, medical and security imaging, and novel analytic and sensing capabilities. Our model for single layer graphene is also expected to be universal, and to hold for a broad variety of systems: in particular, the infrared spectroscopy of bilayer^{10,11} and few-layer⁵¹ graphene, as well as carbon nanotubes,^{30,54,55} should be revisited, as there too shall disorder enable phonon-mediated intra- and intervalley scattering.

Acknowledgement

The authors acknowledge insightful discussions with D. Mayou and G. Antonius, as well as P. Lévesque, who provided also technical assistance. Research described in this paper was partly performed at the Mid-IR beamline of the Canadian Light Source, which is supported by the Natural Sciences and Engineering Research Council of Canada, the National Research Council Canada, the Canadian Institutes of Health Research, the Province of Saskatchewan, Western Economic Diversification Canada, and the University of Saskatchewan. The authors thankfully acknowledge funding from the Natural Sciences and Engineering Research Council of Canada (NSERC), the chaire de recherche de l'Université de Montréal and the Fond de Recherche du Québec - Nature et Technologies (FQRNT). Simulations were performed on the infrastructures of Calcul Québec.

Supporting Information Available

The Supporting Information contains further characterization of the graphene samples, additional results and fits, and a complete description of the model used to compute the optical conductivity. This material is available free of charge via the Internet at <http://pubs.acs.org/>.

Competing Financial Interests

The authors declare no competing financial interests.

References

- (1) Rodrigo, D.; Limaj, O.; Janner, D.; Etezadi, D.; García de Abajo, F. J.; Pruneri, V.; Altug, H. Mid-infrared plasmonic biosensing with graphene. *Science* **2015**, *349*, 165–

168.

- (2) Farmer, D. B.; Avouris, P.; Li, Y.; Heinz, T. F.; Han, S.-J. Ultrasensitive plasmonic detection of molecules with graphene. *ACS Photonics* **2016**, 553–557.
- (3) Low, T.; Avouris, P. Graphene plasmonics for terahertz to mid-infrared applications. *ACS Nano* **2014**, 8, 1086–1101.
- (4) Horng, J.; Chen, C.-F.; Geng, B.; Girit, C.; Zhang, Y.; Hao, Z.; Bechtel, H. A.; Martin, M.; Zettl, A.; Crommie, M. F. et al. Drude conductivity of Dirac fermions in graphene. *Phys. Rev. B* **2011**, 83, 165113.
- (5) Zallen, R. Symmetry and reststrahlen in elemental crystals. *Phys. Rev.* **1968**, 173, 824–832.
- (6) Ju, L.; Geng, B.; Horng, J.; Girit, C.; Martin, M.; Hao, Z.; Bechtel, H. A.; Liang, X.; Zettl, A.; Shen, Y. R. et al. Graphene plasmonics for tunable terahertz metamaterials. *Nat. Nanotechnol.* **2011**, 6, 630–634.
- (7) Yan, H.; Low, T.; Zhu, W.; Wu, Y.; Freitag, M.; Li, X.; Avouris, P.; Xia, F. Damping pathways of mid-infrared plasmons in graphene nanostructures. *Nat. Photonics* **2013**, 7, 394–399.
- (8) Brar, V. W.; Sherrott, M. C.; Sweatlock, L. A.; Jang, M. S.; Kim, L.; Choi, M.; Atwater, H. A. Electronic modulation of infrared emissivity in graphene plasmonic resonators. *Nat. Commun.* **2015**, 6, 7032.
- (9) Yan, H.; Li, X.; Chandra, B.; Tulevski, G.; Wu, Y.; Freitag, M.; Zhu, W.; Avouris, P.; Xia, F. Tunable infrared plasmonic devices using graphene/insulator stacks. *Nat. Nanotechnol.* **2012**, 7, 330–334.
- (10) Kuzmenko, A.; Benfatto, L.; Cappelluti, E.; Crassee, I.; van der Marel, D.; Blake, P.;

- Novoselov, K.; Geim, A. Gate tunable infrared phonon anomalies in bilayer graphene. *Phys. Rev. Lett.* **2009**, *103*, 116804.
- (11) Tang, T.-T.; Zhang, Y.; Park, C.-H.; Geng, B.; Girit, C.; Hao, Z.; Martin, M. C.; Zettl, A.; Crommie, M. F.; Louie, S. G. et al. A tunable phonon-exciton Fano system in bilayer graphene. *Nat. Nanotechnol.* **2010**, *5*, 32–36.
- (12) Yan, H.; Low, T.; Guinea, F.; Xia, F.; Avouris, P. Tunable phonon-induced transparency in bilayer graphene nanoribbons. *Nano Lett.* **2014**, *14*, 4581–4586.
- (13) Low, T.; Guinea, F.; Yan, H.; Xia, F.; Avouris, P. Novel midinfrared plasmonic properties of bilayer graphene. *Phys. Rev. Lett.* **2014**, *112*, 116801.
- (14) Kneipp, K.; Kneipp, H.; Kneipp, J. Probing plasmonic nanostructures by photons and electrons. *Chem. Sci.* **2015**, *6*, 2721–2726.
- (15) Hentschel, M.; Saliba, M.; Vogelgesang, R.; Giessen, H.; Alivisatos, A. P.; Liu, N. Transition from isolated to collective modes in plasmonic oligomers. *Nano Lett.* **2010**, *10*, 2721–2726.
- (16) Lukin, M. D.; Imamoglu, A. Controlling photons using electromagnetically induced transparency. *Nature* **2001**, *413*, 273–276.
- (17) Herzog, J. B.; Knight, M. W.; Li, Y.; Evans, K. M.; Halas, N. J.; Natelson, D. Dark plasmons in hot spot generation and polarization in interelectrode nanoscale junctions. *Nano Lett.* **2013**, *13*, 1359–1364.
- (18) Sibert, E. L.; Hynes, J. T.; Reinhardt, W. P. Fermi resonance from a curvilinear perspective. *J. Phys. Chem.* **1983**, *87*, 2032–2037.
- (19) Snyder, R. G.; Strauss, H. L.; Elliger, C. A. C-H stretching modes and the structure. 1. Long, disordered chains. *J. Phys. Chem.* **1982**, *86*, 5145–5150.

- (20) Rice, M. J. Organic linear conductors as systems for the study of electron-phonon interactions in the organic solid state. *Phys. Rev. Lett.* **1976**, *37*, 36–39.
- (21) Loudon, R. Selection rules for defect-activated lattice bands and vibronic transitions in face-centred cubic, diamond and zinc blende lattices. *Proc. Phys. Soc., London* **1964**, *84*, 379–388.
- (22) Pimenta, M. A.; Dresselhaus, G.; Dresselhaus, M. S.; Cançado, L. G.; Jorio, A.; Saito, R. Studying disorder in graphite-based systems by Raman spectroscopy. *Phys. Chem. Chem. Phys.* **2007**, *9*, 1276–1291.
- (23) Rycerz, A.; Tworzydło, J.; Beenakker, C. W. J. Valley filter and valley valve in graphene. *Nat. Phys.* **2007**, *3*, 172–175.
- (24) Xiao, D.; Yao, W.; Niu, Q. Valley-contrasting physics in graphene: magnetic moment and topological transport. *Phys. Rev. Lett.* **2007**, *99*, 236809.
- (25) Yao, W.; Xiao, D.; Niu, Q. Valley-dependent optoelectronics from inversion symmetry breaking. *Phys. Rev. B* **2008**, *77*, 235406.
- (26) Young, A. F.; Dean, C. R.; Wang, L.; Ren, H.; Cadden-Zimansky, P.; Watanabe, K.; Taniguchi, T.; Hone, J.; Shepard, K. L.; Kim, P. Spin and valley quantum Hall ferromagnetism in graphene. *Nat. Phys.* **2012**, *8*, 550–556.
- (27) Peters, E. C.; Giesbers, A. J. M.; Zeitler, U.; Burghard, M.; Kern, K. Valley-polarized massive charge carriers in gapped graphene. *Phys. Rev. B* **2013**, *87*, 201403(R).
- (28) Kampfrath, T.; Perfetti, L.; Schapper, F.; Frischkorn, C.; Wolf, M. Strongly coupled optical phonons in the ultrafast dynamics of the electronic energy and current relaxation in graphite. *Phys. Rev. Lett.* **2005**, *95*, 187403.
- (29) Thomsen, C.; Reich, S. Double resonant Raman scattering in graphite. *Phys. Rev. Lett.* **2000**, *85*, 5214–5217.

- (30) Lapointe, F.; Gaufres, E.; Tremblay, I.; Tang, N.; Martel, R.; Desjardins, P. Fano resonances in the midinfrared spectra of single-walled carbon nanotubes. *Phys. Rev. Lett.* **2012**, *109*, 097402.
- (31) Han, Z.; Kimouche, A.; Kalita, D.; Allain, A.; Arjmandi-Tash, H.; Reserbat-Plantey, A.; Marty, L.; Pairis, S.; Reita, V.; Bendiab, N. et al. Homogeneous optical and electronic properties of graphene due to the suppression of multilayer patches during CVD on copper foils. *Adv. Funct. Mater.* **2014**, *24*, 964–970.
- (32) Suk, J. W.; Kitt, A.; Magnuson, C. W.; Hao, Y.; Ahmed, S.; An, J.; Swan, A. K.; Goldberg, B. B.; Ruoff, R. S. Transfer of CVD-grown monolayer graphene onto arbitrary substrates. *ACS Nano* **2011**, *5*, 6916–6924.
- (33) Baranton, S.; Bélanger, D. Electrochemical derivatization of carbon surface by reduction of in situ generated diazonium cations. *J. Phys. Chem. B* **2005**, *109*, 24401–24410.
- (34) Gan, L.; Zhang, D.; Guo, X. Electrochemistry: An efficient way to chemically modify individual monolayers of graphene. *Small* **2012**, *8*, 1326–1330.
- (35) Wang, Q. H.; Jin, Z.; Kim, K. K.; Hilmer, A. J.; Paulus, G. L. C.; Shih, C.-J.; Ham, M.-H.; Sanchez-Yamagishi, J. D.; Watanabe, K.; Taniguchi, T. et al. Understanding and controlling the substrate effect on graphene electron-transfer chemistry via reactivity imprint lithography. *Nat. Chem.* **2012**, *4*, 724–732.
- (36) Aguirre, C. M.; Levesque, P. L.; Paillet, M.; Lapointe, F.; St-Antoine, B. C.; Desjardins, P.; Martel, R. The role of the oxygen/water redox couple in suppressing electron conduction in field-effect transistors. *Adv. Mater.* **2009**, *21*, 3087–3091.
- (37) Levesque, P. L.; Sabri, S. S.; Aguirre, C. M.; Guillemette, J.; Siaj, M.; Desjardins, P.; Szkopek, T.; Martel, R. Probing charge transfer at surfaces using graphene transistors. *Nano Lett.* **2011**, *11*, 132–137.

- (38) Lucchese, M.; Stavale, F.; Ferreira, E. M.; Vilani, C.; Moutinho, M.; Capaz, R. B.; Achete, C.; Jorio, A. Quantifying ion-induced defects and Raman relaxation length in graphene. *Carbon* **2010**, *48*, 1592–1597.
- (39) Cançado, L. G.; Jorio, A.; Martins Ferreira, E. H.; Stavale, F.; Achete, C. A.; Capaz, R. B.; Moutinho, M. V. O.; Lombardo, A.; Kulmala, T. S.; Ferrari, A. C. Quantifying defects in graphene via Raman spectroscopy at different excitation energies. *Nano Lett.* **2011**, *11*, 3190–3196.
- (40) Peres, N. M. R.; Guinea, F.; Castro Neto, A. H. Electronic properties of disordered two-dimensional carbon. *Phys. Rev. B* **2006**, *73*, 125411.
- (41) Dubay, O.; Kresse, G. Accurate density functional calculations for the phonon dispersion relations of graphite layer and carbon nanotubes. *Phys. Rev. B* **2003**, *67*, 035401.
- (42) Lazzeri, M.; Attaccalite, C.; Wirtz, L.; Mauri, F. Impact of the electron-electron correlation on phonon dispersion: Failure of LDA and GGA DFT functionals in graphene and graphite. *Phys. Rev. B* **2008**, *78*, 081406.
- (43) Jiang, J.; Saito, R.; Samsonidze, G.; Chou, S.; Jorio, A.; Dresselhaus, G.; Dresselhaus, M. Electron-phonon matrix elements in single-wall carbon nanotubes. *Phys. Rev. B* **2005**, *72*, 235408.
- (44) Niyogi, S.; Bekyarova, E.; Hong, J.; Khizroev, S.; Berger, C.; de Heer, W.; Haddon, R. C. Covalent chemistry for graphene electronics. *J. Phys. Chem. Lett.* **2011**, *2*, 2487–2498.
- (45) Reich, S.; Thomsen, C. Raman spectroscopy of graphite. *Philos. Trans. R. Soc., A* **2004**, *362*, 2271–2288.
- (46) Ferrari, A. C. Raman spectroscopy of graphene and graphite: Disorder, electron-phonon coupling, doping and nonadiabatic effects. *Solid State Commun.* **2007**, *143*, 47–57.

- (47) Mahan, G. D. *Many-particle physics*, 2nd ed.; Plenum Press: New York, 1990; p 1032.
- (48) Mattuck, R. *A guide to Feynman diagrams in the many-body problem*; Dover Books on Physics Series; Dover Publications: New York, 1976; p 429.
- (49) Cappelluti, E.; Benfatto, L.; Kuzmenko, A. Phonon switching and combined Fano-Rice effect in optical spectra of bilayer graphene. *Phys. Rev. B* **2010**, *82*, 041402(R).
- (50) Cappelluti, E.; Benfatto, L.; Manzardo, M.; Kuzmenko, A. B. Charged-phonon theory and Fano effect in the optical spectroscopy of bilayer graphene. *Phys. Rev. B* **2012**, *86*, 115439.
- (51) Li, Z.; Lui, C.; Cappelluti, E.; Benfatto, L.; Mak, K.; Carr, G.; Shan, J.; Heinz, T. Structure-dependent Fano resonances in the infrared spectra of phonons in few-layer graphene. *Phys. Rev. Lett.* **2012**, *108*, 156801.
- (52) Dubé, L.; Herzenberg, A. *Phys. Rev. A* **1979**, *20*, 194–213.
- (53) Piscanec, S.; Lazzeri, M.; Mauri, F.; Ferrari, A.; Robertson, J. Kohn anomalies and electron-phonon interactions in graphite. *Phys. Rev. Lett.* **2004**, *93*, 185503.
- (54) Pekker, Á.; Botos, Á.; Ruzsnyak, Á.; Koltai, J.; Kürti, J.; Kamarás, K. Vibrational signatures in the infrared spectra of single- and double-walled carbon nanotubes and their diameter dependence. *J. Phys. Chem. Lett.* **2011**, *2*, 2079–2082.
- (55) Belhboub, A.; Hermet, P.; Alvarez, L.; Le Parc, R.; Rols, S.; Lopes Selvati, A. C.; Jous-selme, B.; Sato, Y.; Suenaga, K.; Rahmani, A. et al. Enhancing the infrared response of carbon nanotubes from oligo-quaterthiophene interactions. *J. Phys. Chem. C* **2016**, *120*, 28802–28807.

Graphical TOC Entry

